Ru single atom catalyst with dual reaction sites for efficient fenton-like degradation of organic contaminants

Weina Tang [a], Huimin Zhang [a], Xinyi Yang [a], Zhichao Dai [a], Yunqiang Sun [a], Hongmei Liu [c,*], Zunfu Hu [a,b,**], Xiuwen Zheng [a,*]

[a] *Key Laboratory of Functional Nanomaterials and Technology in Universities of Shandong, College of Chemistry and Chemical Engineering, Linyi University, Linyi 276000, PR China*
[b] *School of Materials Science and Engineering, Linyi University, Linyi 276000, PR China*
[c] *School of Physics and Electronic Engineering, Linyi University, Linyi 276000, PR China*

ARTICLE INFO

ABSTRACT

Recently, Fenton-like reaction based on peroxymonosulfate (PMS) has been recognized as a potential alternative for the degradation of organic pollutants. Herein, a high-efficiency and stable catalyst comprised of single Ru atoms dispersed on N-doped carbon (Ru$_{SA}$-N-C) is synthesized by solvothermal strategy. Ru$_{SA}$-N-C could effectively activate PMS for the degradation of azide dyes (Orange II), compared with Ru-nanoparticle-loaded catalysts. Free radical scavenging experiments and density functional theory have displayed that singlet oxygen ($^1O_2$) produced by Ru-N$_4$ sites are the main reactive oxygen species for the degradation of Orange II. Meanwhile, the adjacent pyridinic N acts as the adsorption sites to anchor Orange II. The ultra-high catalytic activity of Ru$_{SA}$-N-C mainly derive from its distinctive dual reaction sites, which significantly shorten the migration distance from $^1O_2$ to the adsorbed Orange II molecules. This study provides a potential Ru$_{SA}$-N-C/PMS system for the high-efficiency sewage treatment.

1. Introduction

Recently, the potential harm of increasing contaminants to ecological environment and human health has been widely concerned, even if their low content in environment.[1,2] Acid orange A (Orange II), a typical azide dyes, are widely applied for textile dyeing, printing and leather processing.[3,4] However, Orange II, with high toxic and refractory, could not be degraded by traditional sewage treatment technologies, for instance adsorption, settlement and biodegradation.[5–7] Based on the Fenton-like reaction, advanced oxidation processes (AOPs) could produce serial reactive oxygen species (ROS), for instance hydroxyl radical (•OH), singlet oxygen ($^1O_2$) and sulfate radical (SO$_4^{\bullet-}$), *etc.* [8] As produced ROS could effectively degrade toxic and refractory contaminants into non-toxic small molecules even CO$_2$ and H$_2$O, realizing the degradation of organic pollutants.[9,10] During the AOPs process, peroxymonosulfate (PMS) is often selected as efficient oxidant, which could be actuated by Fenton-like catalysts.[11–13] Numerous novel catalysts have been developed for PMS activation, including carbon-based nanomaterials[14,15], graphene[16–18], transition metals[19,20] and MOF-based nanomaterials[21–23], *etc.* However, there are several insurmountable defects, for instance low catalytic efficiency, poor stability, secondary metal contamination, low activation efficiency of PMS, greatly hinder its practical applications.[24–26] Hence, it is of great practical significance to prepare novel catalysts to overcome these defects.

Single-atom catalysts (SACs) have been the research hotspot in the field of catalysis due to their ultrahigh atom efficiency, tunable electronic structure, well-identified structures and superior catalytic activities.[27–32] At present, numerous SACs dispersed on nitrogen-doped carbon substrates exhibit prominent performance in serial catalytic reactions, for instance oxygen reduction, CO$_2$ reduction, N$_2$ reduction, *etc.* [33–37] During the treatment of contaminants, the distance between the PMS activation sites and the adsorption sites of organic pollutants is of great significance for the improvement of AOPs.[38] To set PMS activation and organics adsorption at the same or adjacent sites is one of the key strategy to improve the AOPs process.[39–41] Hence, the

**Fig. 1.** (a) Schematic synthesis process of Ru$_{SA}$-N-C. (b) TEM image of Ru$_{SA}$-N-C, (c) SEM image of Ru$_{SA}$-N-C, (d) energy-dispersive spectroscopy (EDS) mapping of Ru$_{SA}$-N-C, (e) HAADF-STEM image of Ru$_{SA}$-N-C. (f) XRD patterns of N-C, Ru$_{SA}$-N-C and Ru$_{NP}$-N-C. (g) Raman spectrum of N-C, Ru$_{SA}$-N-C and Ru$_{NP}$-N-C.

emergence of SACs is expected to reduce the distance between PMS activation sites and adsorption sites during the AOPs process. For instance, based on the adjacent PMS activation and organic pollutants adsorption sites, cobalt single atom catalysts (Co-N-C) could completely degrade phenol in 20 min.[42] Coincidentally, a powerful Mn SACs was prepared with nitrogen-doped carbon as substrates, which exhibited excellent PMS activation activity.[43] During the process of catalytic degradation of Bisphenol A, monodisperse Mn-N$_4$ sites were applied to activate PMS, while the adjacent pyrrolic N sites severed as adsorption sites for Bisphenol A. Although several SACs-based Fenton-like catalysts have been applied for the degradation of contaminants, but the exact catalytic mechanism and catalytic performance needs to be further studied.

In this work, a high-efficiency and stable catalytic system was constructed based on the atomically dispersed Ru catalyst (Ru$_{SA}$-N-C). Ru$_{SA}$-

N-C was employed for the degradation of azide dyes (Orange II) for the first time. The experimental results and density functional theory (DFT) calculations revealed that the atomically dispersed Ru-nitrogen sites (RuN$_4$) served as the active sites of PMS activation. Additionally, the adjacent pyridinic N was applied for the adsorption of Orange II. Free radical scavenging experiments and electron paramagnetic resonances confirmed that $^1O_2$ was the main ROS for the degradation of Orange II. In addition, the adjacent dual reaction sites significantly shorten the distance between ROS and Orange II, thus, it significantly improved the catalytic capacity of Ru$_{SA}$-N-C, facilitating the degradation of Orange II. The mineralization degree of Ru$_{SA}$-N-C/PMS system was determined by total organic carbon analysis. This study opens a novel avenue for the construction of SACs-based AOPs catalysts for water treatment.
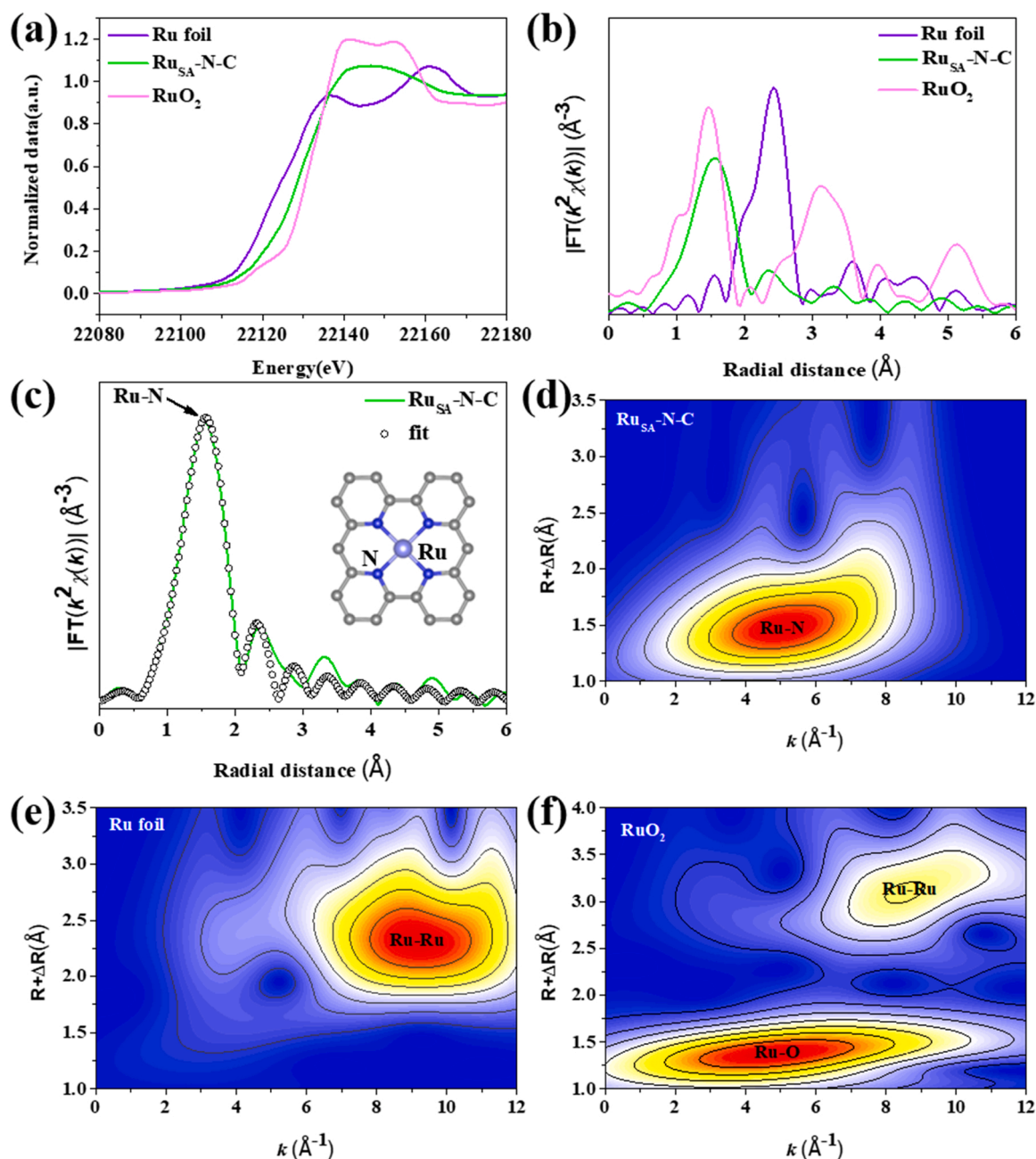
Fig. 2. (a) Ru K-edge XANES spectrum of Ru_{SA}-N-C. (b) R-space spectrum from EXAFS for the Ru_{SA}-N-C, Ru foil and RuO_2. (c) Corresponding Ru K-edge EXAFS fitting curves of Ru_{SA}-N-C (inset: optimized model of Ru_{SA}-N-C). Wavelet transform (WT) of (d) Ru_{SA}-N-C, (e) Ru foil, and (f) RuO_2.

2. Experimental section

2.1. Synthesis of Ru_{SA}-N-C

To prepare the Ru_{SA}-N-C catalyst, we first prepared N-C catalyst. Briefly, Zn $(NO_3)_2 \cdot 6H_2O$ (1.7849 g, 6 mmol) was dissolved in 50 ml methanol and subsequently added into 50 ml methanol containing 2-methylimidazole (2.9556 g, 36 mmol) under vigorous stirring for 30 min at 25 °C. Next, the mixed solutions were poured into a 200 ml Teflon-lined stainless-steel autoclave and then heated at 120 °C for 4 h. After cooling down to room temperature, the obtained precipitate was collected by centrifuged and washed with methanol three times, finally dried at 60 °C under vacuum overnight (the obtained powder was labeled as ZIF-8). Afterwards, the powder of ZIF-8 was put into a tube furnace for pyrolysis under 1000 °C for 2 h with a heating rate of 4 °C

min^{-1} under flowing argon to obtain the N-C. For metal doping, N-C (50 mg), Ru(acac)$_3$ (19.92 mg) and dicyandiamide (100 mg) were adding into a mixture of water (15 ml) and isopropyl alcohol (15 ml), followed by vigorous sonication for 3 h and stirring for 4 h at room temperature. Then, the obtained sample was dried at 70 °C under vacuum overnight and annealed at 600 °C for 2 h in Ar atmosphere. Finally, Ru_{SA}-N-C were obtained. The Ru_{NP}-N-C was prepared with the same procedure except for adding 200 mg Ru(acac)$_3$ to form particle of Ru instead of single atoms.

2.2. Catalytic oxidation experiments

The degradation experiments were carried out in 200 ml round bottom flasks. During this process, a constant temperature water bath was used to maintain the temperature of the reaction vessel. H_2SO_4 (1
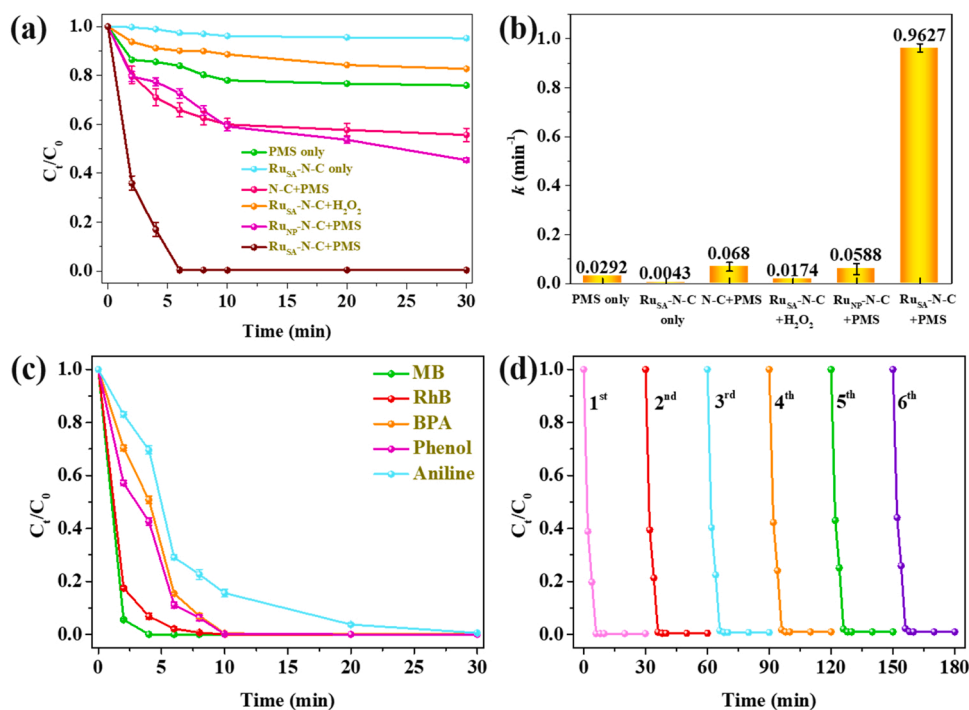
Fig. 3. (a) Fenton-like catalytic performance for various catalysts under the same condition. [Orange II]$_0$ = 50 mg/L, [PMS]$_0$ = 1 g/L, [catalyst]$_0$ = 0.1 g/L, pH= 6.0, 25 ℃). (b) corresponding rate constant. (c) Substrate expansion of Ru$_{SA}$-N-C/PMS system. (the conditions are the same as Fig. 3a). (d) Cyclic catalysis experiment of Ru$_{SA}$-N-C.

M) and NaOH (0.5 M) were used to adjusted the initial pH of the solution. In a typical run, Orange II solution (100 ml) with different initial concentrations (0.03–0.09 g/L) were transferred into round bottom flasks, and then certain amount of catalyst (0.01–0.2 g/L) were added to the pollutant solution. The solution was stirred for 30 min to achieve the adsorption-desorption equilibrium. Then, PMS (0.1–1.0 g/L) was added to initiate the test. 2.0 ml of the obtained solution was collected with a syringe at a specific time point, immediately burst with excess methanol and filtered through a 0.22 μm Teflon filter. The UV absorption at 484 nm was subsequently measured by UV–visible spectrophotometer. For comparison, hydrogen peroxide (H$_2$O$_2$) as an alternative oxidant was also inquired under the same conditions. Besides, other organic pollutants including phenol, Methylene Blue (MB), Bisphenol A (BPA), Rhodamine B (Rh B) and aniline were also investigated.

3. Results and discussion

3.1. Preparation and Structural Analysis of As-fabricated Catalysts

The synthetic strategy of Ru$_{SA}$-N-C was presented in Fig. 1a. Firstly, ZIF-8 was synthesized by solvothermal method (Fig. S1 and S2). Then, the obtained powder was pyrolyzed at 1000 ℃ (denoted as N-C). Defects and microporous structures were produced after the evaporation at 1000 ℃. Secondly, atomically dispersed Ru sites were introduced via a secondary pyrolysis strategy. After the secondary pyrolysis under Ar atmosphere, atomically dispersed Ru sites were fixed on N-doped carbon, forming Ru$_{SA}$-N-C catalyst. For comparison, Ru-nanoparticle-loaded catalysts (Ru$_{NP}$-N-C) were synthesized by the same preparation method except that the amount of Ru(acac)$_3$ precursors was ten times of Ru$_{SA}$-N-C.

Various characterizations were employed to confirm the formation of Ru$_{SA}$-N-C. TEM and SEM (Fig. 1b, c) images showed that Ru$_{SA}$-N-C had a typical rhombic dodecahedron shape and a uniform size, which was consistent with the N-C carrier (Fig. S3). The energy-dispersive spectroscopy (EDS) mapping showed that Ru, C and N were distributed homogeneously throughout the architecture, as illustrated in Fig. 1d.

The atomically dispersed Ru atoms anchored on the N-doped carbon substrates could be clearly observed by HAADF-STEM, marked by red cycles (Fig. 1e). The X-ray powder diffraction (XRD) spectra of Ru$_{SA}$-N-C and N-C showed one diffraction peak at around 23°, assigning to (002) plane of graphitic (Fig. 1f). In addition, no other crystalline forms of Ru were found in the XRD spectra, confirming that no clusters or nanoparticles were presented. Compared with Ru$_{SA}$-N-C and N-C, the appearance of Ru nanoparticle absorption peak confirmed the formation of nanoparticles, consistent with the TEM and HAADF-STEM results (Fig. S4).

The accurate Ru content of Ru$_{SA}$-N-C was measured as 0.35 wt% using inductively coupled plasma-optical emission spectrometry (ICP-OES) (Table. S3). Raman spectrum was also performed to analyze the structure of as-fabricated catalysts. N-C, Ru$_{NP}$-N-C and Ru$_{SA}$-N-C exhibited similar D/G-band intensity, indicating graphite-like structure (Fig. 1g). The specific surface areas of Ru$_{SA}$-N-C and Ru$_{NP}$-N-C were calculated to be 750.16 m^2 g^{-1} and 734.7 m^2 g^{-1} based on the Brunauer-Emmett-Teller measurements, which were favorable for the adsorption of organics and persulfate (Fig. S5). X-ray photoelectron spectroscopy (XPS) was employed to analyze the chemical state of Ru, N and C in Ru$_{SA}$-N-C. As depicted in Fig. S6a, the survey XPS spectrum presented peaks of Ru, N and C. In addition, the high-resolution N1s spectra of Ru$_{SA}$-N-C were divided into three peaks, indicating that there were mainly pyridinic N (58.37%), pyrrolic N (24.12%) and graphitic N (17.51%) after carbonization (Fig. S6c). Notably, the highly defective pyridinic N and pyrrolic N facilitated the immobilization of Ru atoms. [44] Meanwhile, the C-N peak around 284.2 eV was presented in the C 1 s spectra of Ru$_{SA}$-N-C, indicating the successful formation of N-doped carbon substrates with considerable defects (Fig. S6d).

X-ray absorption near-edge structure (XANES) and extended X-ray absorption fine structure (EXAFS) spectroscopy were applied to further study the chemical state and coordination environments of isolated Ru atoms in as-prepared Ru$_{SA}$-N-C catalyst. As depicted in Fig. 2a, Ru K-edges XANES profile revealed that the edge energy (E0) value of Ru$_{SA}$-N-C located between Ru foil and RuO$_2$, demonstrating that the valence state of Ru species was positive in Ru$_{SA}$-N-C. Furthermore, the Ru K-edge

EXAFS spectrum of Ru$_{SA}$-N-C catalysts were employed to investigate the coordination environment of Ru. As illustrated in Fig. 2b, the R-space spectra of Ru$_{SA}$-N-C exhibited strong peak around 1.6Å, assigning to Ru-N scattering path. In addition, no distinct Ru-Ru peaks were found in the K-edge EXAFS spectrum, further verifying the dominant presence of isolated Ru atoms. The EXAFS fitting curves were also employed to study the coordination environment of Ru sites in Ru$_{SA}$-N-C. As depicted in Fig. 2c and Tab. S1, the coordination number of Ru atom was calculated to be 4 based on the fitting results. EXAFS wavelet transforms (WT) was employed to confirm above results (Fig. 2d-f), distinguishing backscattered atoms in K and R Spaces at high resolution. As illustrated in Fig. 2d, compared with Ru foil and RuO$_2$, there was a maximum absorption peak around 5.2 Å^{-1} in the WT plots of Ru$_{SA}$-N-C, consistent with the Ru-N coordination. Based on the high consistency of XAFS test and theoretical calculation, the optimum structural model of Ru$_{SA}$-N-C was illustrated in the insert of Fig. 2c.

3.2. Catalytic performance of Ru$_{SA}$-N-C among advanced oxidation processes

Orange II was employed as the contaminants to compare the catalytic performance between N-C, Ru$_{NP}$-N-C and Ru$_{SA}$-N-C. All samples with Orange II were stirred 30 min to reach adsorption-desorption equilibrium. As depicted in Fig. 3a, as-prepared catalysts displayed different catalytic performances for Orange II degradation. The Fenton-like degradation efficiency of Ru$_{SA}$-N-C, Ru$_{NP}$-N-C and N-C reached 100%, 54.6% and 40.63% within 30 min, respectively. The kinetics was calculated based on the pseudo-first-order kinetics model: $\ln(C_t/C_0) = -kt$, where C_0 and C_t represent the organic matter concentrations at time t = 0 and t, respectively, and k (min^{-1}) is the reaction rate constant.[41] The apparent reaction rate constant k was 0.0588 min^{-1} for Ru$_{NP}$-N-C, while 0.9627 min^{-1} for Ru$_{SA}$-N-C, indicating Ru$_{SA}$-N-C exhibited higher catalytic activity. As displayed in Fig. 3a, only 24.24% Orange II were degraded by PMS within 30 min without catalysts, indicating that insufficient ROS was generated by PMS activation. When only Ru$_{SA}$-N-C was added, Orange II concentration hardly changed with only 4.67% Orange II was adsorbed. In contrast, in the presence of Ru$_{SA}$-N-C and PMS, the degradation efficiency could reach 100% within 30 min, while the mineralization degree, characterized by TOC removal, reached 34.49% (Fig. S10-11). For comparison, only 17.29% of Orange II was degraded within 30 min catalyzed by Ru$_{SA}$-N-C/H$_2$O$_2$ (Fig. 3a). As illustrated in Fig. 3b, the corresponding kinetics was calculated to be 0.9627 min^{-1}, indicating that Ru$_{SA}$-N-C could efficiently activate PMS to realize effective degradation of contaminants. In addition, as illustrated in Tab. S2 and S3, the catalytic performance of as-prepared Ru$_{SA}$-N-C catalytic system was better than that of most reported single atom catalytic systems.

3.2.1. Effect of reaction participant concentration on the catalytic degradation of Orange II

The influences of catalyst and PMS concentration on contaminants degradation were inspected systematically (Fig. S12-S13). With the catalyst dosage increased from 0.01 to 0.1 g/L, the catalytic degradation efficiency climbed from 21% to 100% in 30 min, exhibiting a typical concentration dependence. Meanwhile, kinetic rate constant (k) raised from 0.0169 to 0.4733 min^{-1} with the increase of catalysts concentration (Fig. S12b), indicating that more Ru-N$_4$ sites participated in PMS adsorption and activation. However, when catalyst concentration was higher than 0.1 g/L, the degradation efficiency dose not proportional to the increase of catalyst. Obviously, PMS content would greatly affect ROS production (SO$_4^{\bullet-}$, $\bullet$OH, O$_2^{\bullet-}$ and ^{1}O$_2$).[41] The Orange II degradation efficiency raised from 80.83% to 100% in 30 min as PMS concentration increased from 0.1 to 1 g/L. Meanwhile, as depicted in Fig. S13b, k climbed from 0.0551 to 0.9627 min^{-1}. Therefore, the catalyst and PMS concentration were selected as 0.1 and 1 g/L for subsequent experiments, respectively.

The influence of Orange II concentrations on the degradation reaction of Ru$_{SA}$-N-C/PMS system were also investigated. When the concentration of Orange II solution increased to 90 mg/L, it could still be completely degraded in 30 min (Fig. S14a). As depicted in Fig. S14b, the corresponding k decreased from 1.23 to 0.1131 min^{-1}. This might be due to that excessive Orange II might occupy active sites on the surface of Ru$_{SA}$-N-C and weaken the degradation ability. Therefore, after comprehensive consideration, Orange II with medium concentration (50 mg/L) was selected for the next degradation experiment.

3.2.2. Effect of pH and temperature on the catalytic degradation of Orange II

It is well known that pH and temperature have great influence on the catalytic reaction.[45–47] As shown in Fig. S15, when the pH is varied in the range of 4–10, it can be completely degraded within 30 min, suggesting that the as-constructed Ru$_{SA}$-N-C/PMS system exhibits excellent performance for Orange II decomposition in a wide pH range, surpassing traditional Fenton catalysts. As depicted in Fig. S15b, the corresponding k ranged from 0.1147 to 0.9627 min^{-1}. However, most organic contaminants existed in weak acidic environment and PMS/Ru$_{SA}$-N-C system possessed the highest k. Therefore, pH = 6 was selected for subsequent experiments. As temperature raised from 15 to 65 ℃, degradation efficiency of organic matter gradually increased (Fig S16a). Meanwhile, k increased from 0.2334 to 1.1589 min^{-1}, which might attribute to the easy activation of PMS at higher temperature (Fig S16b). In consideration of practical application, 25 ℃ was selected for the following experiments.

3.2.3. Effect of inorganic anion and natural organic matters (NOMs)

Serial inorganic anions (Cl$^-$, H$_2$PO$_4^-$, SO$_4^{2-}$, HCO$_3^-$, and NO$_3^-$) exist in sewage, which might interfere with the catalytic reaction. Therefore, it is of great significance to understand the influence of natural inorganic matter on SACs-based AOPs. As displayed in Fig. S17a, Cl$^-$, H$_2$PO$_4^-$, SO$_4^{2-}$, and NO$_3^-$ exhibited a negligible influence on Orange II degradation. However, when 20 mM HCO$_3^-$ was added, Orange II degradation efficiency decreased to 59.95% and the corresponding k decreased to 0.0846 min^{-1}, as illustrated in Fig. S17b. This might due to the reaction between HCO$_3^-$ and ^{1}O$_2$.[48] In addition, natural organic matters (NOMs) are the main competitor among the degradation of organic pollutants. Humic acid (HA), as a typical NOMs, was employed to study the effect of NOMs on the AOPs process. When HA was added, the catalytic degradation efficiency decreased from 100% to 94.82% in 30 min, which might attribute to the competitive adsorption between HA and Orange II on Ru$_{SA}$-N-C. Meanwhile, k decreased from 0.9627 to 0.1624 min^{-1} (Fig. S17b), indicating that NOMs could remove oxide substrates and reduce the oxidation capacity.

Tap water and lake water containing Orange II were applied to investigate the influence of other factors in the actual water sewage. As depicted in Fig. S18, the Orange II degradation efficiency decreased from 100% in deionized water and tap water to 89.96% in lake water. The inhibition would be ascribed to the effects of co-existing anions and natural organic matters in the actual water.[23,49] However, it is found that the Orange II degradation efficiency returned to 100%, if the Ru$_{SA}$-N-C dosage increased from 0.1 g/L to 0.15 g/L [23]. Furthermore, a self-developed fixed-bed reactor was constructed to verify the possibility in practical application of Ru$_{SA}$-N-C, in which Ru$_{SA}$-N-C and quartz sand were packed in the condenser pipe. The velocities of the Orange II and PMS flows were controlled by peristaltic pump and syringe pump, respectively. As shown in Fig. S19, the long-term Orange II degradation was achieved, without obvious decrease of degradation efficiency even up to 60 min

3.2.4. Degradation of different pollutants by Ru$_{SA}$-N-C/PMS system

The wide adaptability of catalysts is one of the keys to the popularization and application of Ru$_{SA}$-N-C/PMS system. Hence, as-constructed Ru$_{SA}$-N-C/PMS system was employed for the degradation of other
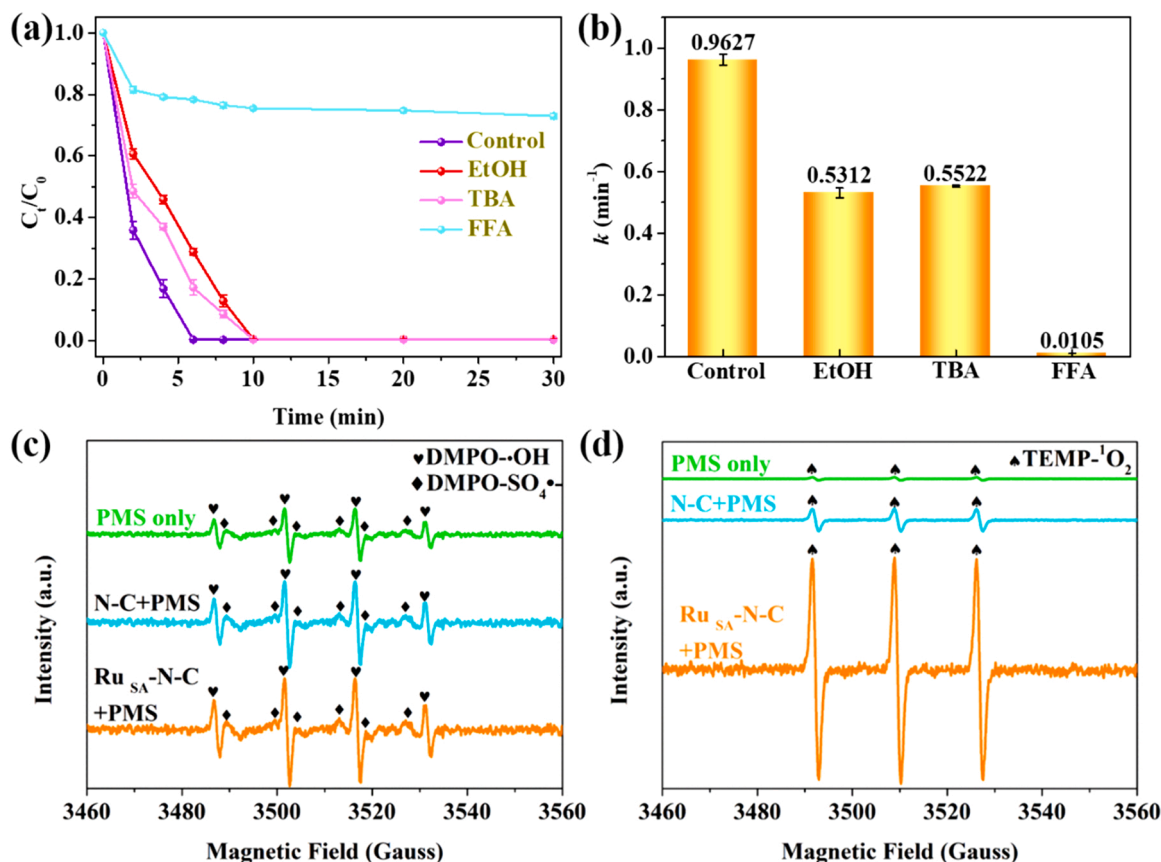
Fig. 4. (a) Ru_{SA}-N-C/PMS system treated with different scavenging agents, and (b) corresponding rate constants. (c) DMPO-trapped and (d) TEMP-trapped EPR spectrum of the PMS, N-C/PMS, and Ru_{SA}-N-C/PMS systems, ◆ represents DMPO-$SO_4^{\bullet-}$, ♥ represents DMPO-$\bullet$OH and ♠ represents TEMP-$^1O_2$. (the reaction conditions are the same as Fig. 3a. [Et]=0.5 M, [TBA]=0.5 M, [FFA]=0.5 M).

organic pollutants, for instance methylene blue, Rhodamine B, Bisphenol A, phenol and aniline. As illustrated in Fig. 3c, methylene blue, Rhodamine B, Bisphenol A and phenol could be completely degraded within 4 min, 8 min, 10 min and 10 min, respectively. Nevertheless, aniline could be completely degraded in 30 min. Above experimental results indicated that Ru_{SA}-N-C exhibit excellent catalytic activity towards various organic pollutants.

3.2.5. Stability and reusability of Ru_{SA}-N-C catalysts and metal ions leaching studies

Cyclic degradation experiments were applied to assess the stability and reusability of Ru_{SA}-N-C/PMS system, which were critical to the practical application of AOPs technology. After each cycle of reaction, Ru_{SA}-N-C was washed with water and collected by centrifugation, then dried for the next experiment. After six cycles, it was found that the catalytic degradation ability of Ru_{SA}-N-C remained almost unchanged (Fig. 3d). In addition, the structure of used catalyst remained unchanged characterized by TEM and XRD, further confirming the outstanding recyclability and stability of Ru_{SA}-N-C (Fig. S20-S21). Furthermore, ICP-OES was employed for the detection of metal ions leaching after each cyclic degradation experiment. As illustrated in Fig. S22, negligible Ru ions were released from Ru_{SA}-N-C during the Fenton-like process, indicating that as-prepared Ru_{SA}-N-C could effectively inhibit secondary metal contamination.

3.2.6. Mechanism of catalytic degradation

It is well known that free radical and/or non-free radical oxidation was confirmed involved the AOPs process. The generated ROS, for instance $SO_4^{\bullet-}$, $\bullet$OH, $O_2^{\bullet-}$ and $^1O_2$, exhibited excellent oxidation ability, which could oxidize organic pollutants to smaller molecule

intermediates and finally to CO_2 and H_2O.[50–53] To explore the dominant ROS for Orange II degradation in Ru_{SA}-N-C/PMS system, serial scavengers were applied for the trapping experiment. According to the report, the reaction rate of ethanol with $\bullet$OH ($1.2–2.8 \times 10^9$ M^{-1} s^{-1}) was equivalent to that of $SO_4^{\bullet-}$ ($1.6–7.7 \times 10^7$ M^{-1} s^{-1}), while tertiary butanol (TBA) reacted faster with $\bullet$OH ($3.8–7.6 \times 10^8$ M^{-1} s^{-1}) than $SO_4^{\bullet-}$ ($4.0–9.1 \times 10^5$ M^{-1} s^{-1}).[54] Consequently, TBA was employed to trap $\bullet$OH, while ethanol was employed for the trapping of $\bullet$OH and $SO_4^{\bullet-}$.[55] As illustrated in Fig. 4a, the addition of 0.5 M TBA (EtOH) caused a slight decrease of the catalytic degradation efficiency of Ru_{SA}-N-C/PMS system, indicating that $\bullet$OH ($SO_4^{\bullet-}$) played a secondary role in the degradation of Orange II. With DMPO (5, 5-dimethyl-1-pyrroline n-oxide) as trapping agent, electron paramagnetic resonance (EPR) spectra clearly proved the coexistence of $\bullet$OH and $SO_4^{\bullet-}$ in the Ru_{SA}-N-C/PMS system (Fig. 4c). Furthermore, as a typical $^1O_2$ scavenger, when 0.5 M furfuryl alcohol (FFA) was added, the degradation efficiency reduced to 26.09%, confirming that the degradation of Orange II was mainly caused by $^1O_2$ (Fig. 4a). The corresponding k was 0.0105 min^{-1}, as depicted in Fig. 4b. Furthermore, a typical 1:1:1 triplet signal assigned to $^1O_2$ was found in the EPR spectra, indicating the existence of $^1O_2$, as illustrated in Fig. 4d. The degradation efficiency of Orange II remained unchanged in the presence of N_2 (Fig. S23), indicating that $^1O_2$ mainly derived from the decomposition of PMS rather than the external O_2. For Ru_{SA}-N-C/PMS system, the effective utilization of PMS is of great significance to enhance the degradation efficiency of pollutants. As depicted in Fig. S24, 45.32% PMS was consumed in 10 min. The excessive dose of PMS was also confirmed by Orange II degradation curve (Fig. S14 (a)), indicating that more organic pollutants could be completely oxidized.

Nitrogen doping is considered as an important means to optimize
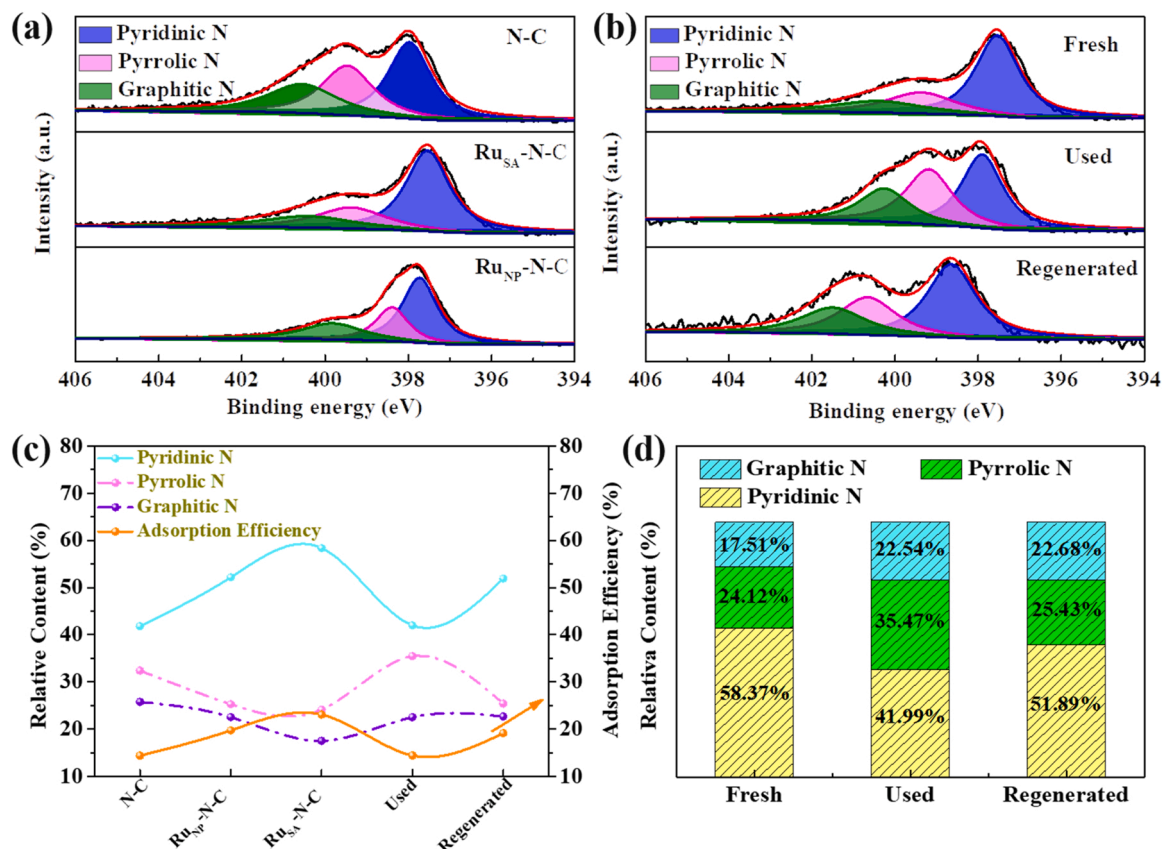
Fig. 5. (a) High-resolution N 1 s XPS spectra for N-C, Ru$_{SA}$-N-C and Ru$_{NP}$-N-C. (b) High-resolution N 1 s XPS spectra for fresh, used and regenerated Ru$_{SA}$-N-C. (c) Relationships of the N species content and Orange II adsorption efficiency for N-C, Ru$_{NP}$-N-C, fresh, used and regenerated Ru$_{SA}$-N-C. (d) The graphitic N, pyrrolic N and pyridinic N contents under different conditions.
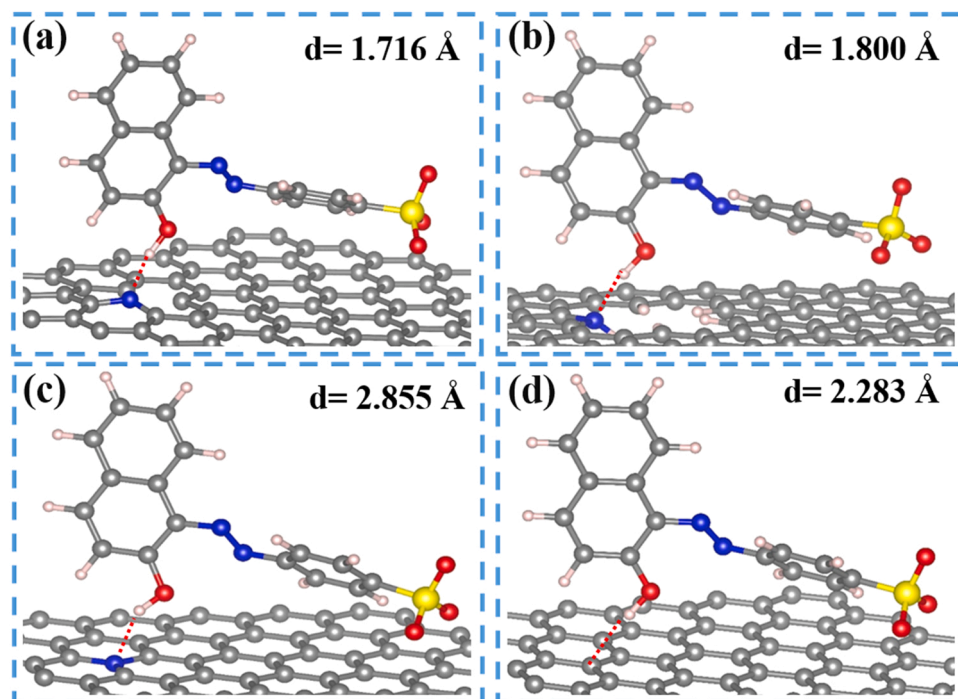
Fig. 6. Optimized adsorption configurations of Orange II on a) pyridinic N, b) pyrrolic N, c) graphitic N and d) graphene (The corresponding distances between N and H atoms are shown in each panel).
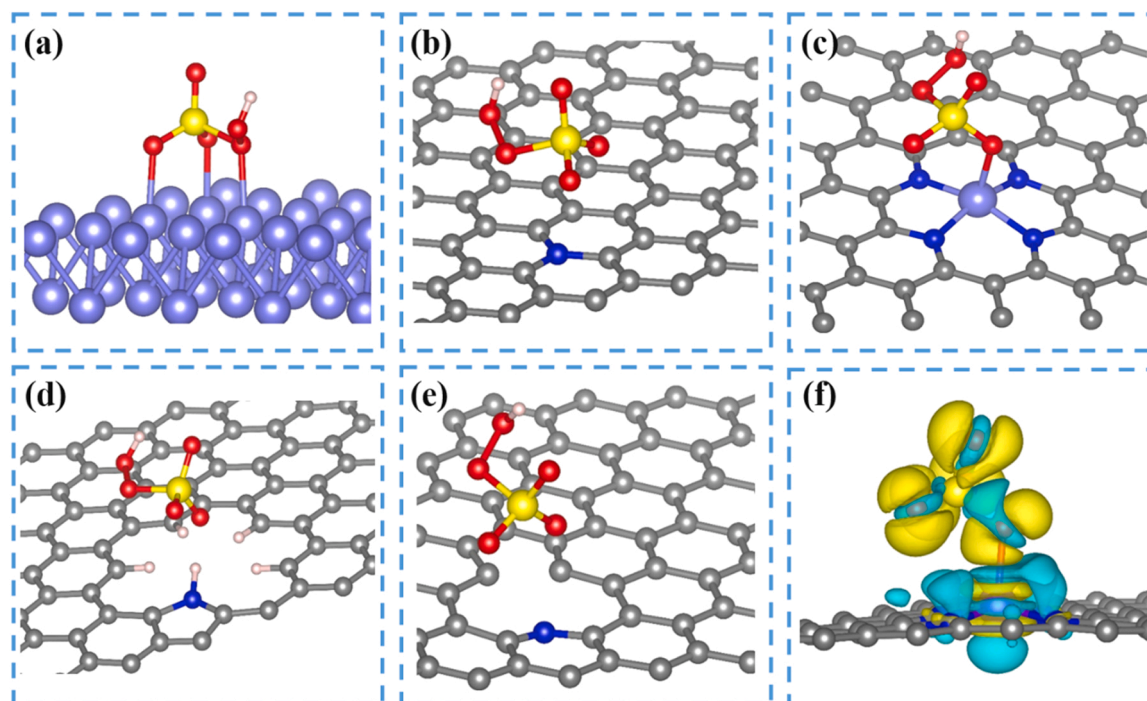
Fig. 7. Optimized adsorption configurations of the PMS molecule on a) Ru, b) graphitic N, c) Ru-N$_4$ d) pyrrolic N, and e) pyridinic N. f) Charge density difference in the RuN$_4$/graphene model. The light yellow represents electron accumulation and the light blue denotes electron depletion. The isosurface value of charge density is 0.0012 e/Bohr^3.

catalytic activity of catalysts.[56] X-ray photoelectron spectroscopy (XPS) was employed to investigate the chemical state of N among those fresh, used and regenerated catalysts. The N1s spectrum of N-C, Ru$_{SA}$-N-C and Ru$_{NP}$-N-C were deconvoluted into three peaks, appointed to pyridinic N (398.6 ± 0.6 eV), pyrrolic N (399.4 ± 0.6 eV), and graphitic N (400.8 ± 0.6 eV) (Fig. 5a-b). To determine the adsorption sites of Orange II, the relationship between the relative content of N and the adsorption efficiency was established and listed in Fig. 5c. It was easy to find that the content of pyridinic N among those catalysts was consistent with the adsorption efficiency of Orange II, indicating that pyridinic N might be the functional sites for the adsorption of Orange II. In addition, when experienced Fenton-like reaction, the content of pyridinic N decreased significantly from 58.37 % to 41.99 %, while the adsorption efficiency of Orange II decreased from 23.10 % to 10.43 % (Fig. 5c, d). After annealing, the adsorption efficiency of Orange II recovered from 10.43 % to 21.03 %, and the content of pyridinic N increased from 41.99 % to 51.89 %, further confirmed the adsorption of pyridinic N. It was believed that the adsorbed Orange II on pyridinic N conformed to the donor-acceptor mechanism, while pyridinic N acted as the electron donor and adsorbed the -OH of Orange II, acting as the electron acceptor (Fig. S25).[43]

Density functional theory (DFT) calculations were applied to reveal the adsorption mechanism and advantages of pyridinic N during the degradation process of Orange II. The optimized adsorption structure and top view of Orange II on graphitic N, pyridinic N, pyrrolic N and graphene were depicted in Fig. 6 and Fig. S29, respectively. According to DFT calculation (Tab. S6 and S7), when Orange II was adsorbed onto pyridinic N, the adsorption energy reached the maximum (1.307 eV) with the shortest OH-N bond (1.716 Å) among several possible adsorption sites. The above calculation results were consistent with the experimental results.

3.3. Orange II degradation pathways

The Fukui function (f_k^0) was usually used to determine the most vulnerable sites of Orange II in the presence of active substances.

Fig. S26 and Tab. S5 exhibited the Fukui index for the different reactive sites of Orange II. ROS tend to attack the sites, which possessed higher Fukui index.[41] The results presented that O10 (f^- = 0.08575), C11(f^- = 0.09194), N13(f^- = 0.08887) and C17(f^- = 0.09697) of Orange II were the most favorable sites for ROS attack. Furthermore, to further comprehend the intermediates and degradation pathways, the reaction solutions were analyzed by liquid chromatography mass spectrometry (LC-MS). Based on LC-MS result (Fig. S27) and literature reports, a possible degradation pathway for Orange II was illustrated in Fig. S28. [57,58] Firstly, the azo bond (-N═N-) was broken and Orange II was decomposed into aromatic intermediates sodium sulfanilamide (Route I (A)) and 1-amino-2-naphthol (Route II (B)). For Route I, sodium sulfanilamide was degraded to hydroquinone (C). Hydroquinone was further oxidized to cyclopenta-2,4-dien-1-ol (D). For Route II, 1-amino-2-naphthol was oxidized to 1,2-naphthalenediol (E). Secondly, 1,2-naphthalenediol (E) was further oxidized to heterocyclic, consisting of a five-atom ring that conclude ninhydrin (F) and 1 (3 H)-isobenzofuranone (G). Finally, the rings of aromatic intermediates were opened, forming various small molecule organic acids, which were eventually oxidized to CO$_2$ and H$_2$O.

3.4. DFT calculations

DFT calculations were employed to further reveal the mechanism of PMS activation and Orange II decomposition. Based on the Sabatier principle, bonding strength between catalyst and reactant should be moderate. Too weak bonding strength does not facilitate the activation of PMS, while too strong bonding strength is unfavorable for desorption of decomposition product.[59] Hence, It is meaningful to calculate the adsorption energy between PMS and RuN$_4$ sites for exploring the catalytic degradation mechanism of Ru-N-C/PMS system. Optimized adsorption configurations of PMS on Ru, graphitic N, Ru-N$_4$, pyrrolic N, pyridinic N and graphene sites were established and listed in Fig. 7a-e, and the corresponding adsorption energies (E$_{ads}$) were shown in Tab. S8. It was easy to find that the adsorption energies of PMS on Ru (3.216 eV) and graphitic N sites (2.919 eV) were so strong that those active sites
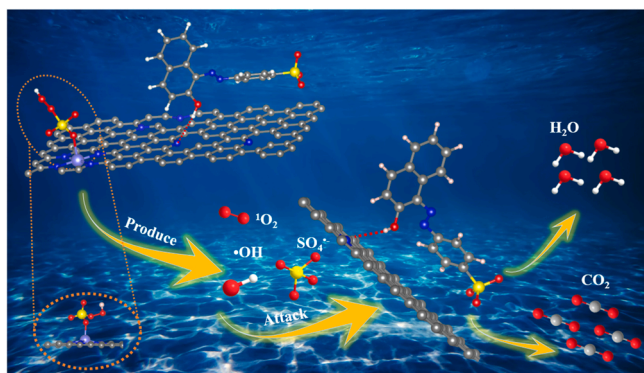
Fig. 8. The proposed mechanism for the Fenton-like degradation on the Ru_{SA}-N-C.

might be poisoned.[60] On the contrary, the adsorption energies of PMS on pyrrolic N (1.217 eV), pyridinic N (1.414 eV) and graphene sites (0.650 eV) were too weak to trigger the activation of PMS. When PMS was bonded onto the Ru-N_4 sites, the adsorption energy was 2.748 eV with a moderate intensity. Therefore, Ru-N_4 sites was regarded as the ideal active site for the activation of PMS according to the Sabatier principle. This might be the reason for the higher catalytic degradation efficiency of Ru_{SA}-N-C than pure N-C. Furthermore, charge density difference plots proved that there was an obvious electron transfer process between Ru-N_4 and PMS, which facilitated the activation of PMS (Fig. 7f). The corresponding top view was shown in Fig. S30. The above studies indicated that the Ru-N_4 sites were the main active sites for the activation of PMS.

Based on the experimental results and DFT calculations, the possible degradation mechanism of Orange II was illustrated as follows (Fig. 8). (1) PMS was adsorbed onto the RuN_4 sites with moderate bonding energy, triggering effective activation of PMS and generating a number of ROS ($^1O_2$, •OH and $SO_4^{•-}$, $^1O_2$ plays a major role). (2) Orange II was adsorbed on the surface of the pyridinic N sites through a donor-acceptor mechanism. The migration distance of $^1O_2$ for one-half-life period was around 90 nm in the reaction solution; [61] therefore, the dual reaction sites within the Ru_{SA}-N-C catalyst shall greatly reduce the migration distance of the active $^1O_2$. As a result, the rapid reaction of generated $^1O_2$ with adjacent adsorbed Orange II on Ru_{SA}-N-C catalyst gives rise to excellent Fenton-like catalytic performance. As a result, the in situ generated active species can react rapidly with the neighboring adsorbed contaminants on Ru_{SA}-N-C, thus significantly improving the Fenton-like catalytic performance.

4. Conclusion

In a word, isolated Ru atom catalyst was prepared via a facile strategy and employed for the degradation of organic contaminants in this work. Ru_{SA}-N-C exhibited remarkable Fenton-like catalytic activity in the degradation of Orange II by activated PMS. As-prepared Ru_{SA}-N-C catalyst exhibited 100% degradation efficiency for Orange II in 6 min with a degradation rate constant of 0.9627 min^{-1}, which was 16 times higher than that of Ru_{NP}-N-C (0.0588 min^{-1}). The experimental results and DFT calculations demonstrated that Ru_{SA}-N-C catalyst possesses abundant $RuN4$ sites, which could efficiently activate PMS for the production of ROS (mainly $^1O_2$). In the meantime, the adjacent pyridinic N sites acted as the adsorption sites for Orange II with a moderate bonding energy. The dual reaction sites of as-prepared Ru_{SA}-N-C catalyst greatly shorten the migration distance between the ROS and Orange II, which significantly improved the catalytic performance of Ru_{SA}-N-C, facilitating the degradation of Orange II without secondary metallic pollution. This successful demonstration of atomically dispersed Ru catalyts for the degradation of organic contaminants may provide highly promising protocols for water-treatment.

CRediT authorship contribution statement

Weina Tang: Data analysis, Investigation, Writing – original draft, Writing – review & editing. **Huimin Zhang:** Formal analysis, Investigation. **Xinyi Yang:** Investigation. **Zhichao Dai:** Writing – review & editing. **Yunqiang Sun:** Writing – review & editing. **Hongmei Liu:** Software, Methodology. **Zunfu Hu:** Writing – review & editing, Methodology. **Xiuwen Zheng:** Conceptualization, Funding acquisition. Supervision, Project administration, Writing – review &editing.

Appendix A. Supporting information

Supplementary data associated with this article can be found in the online version at doi:10.1016/j.apcatb.2022.121952.

References

[1] Q. Dai, Z. Zhang, J. Yan, J. Wu, G. Johnson, W. Sun, X. Wang, S. Zhang, W. Zhan, Phosphate-functionalized CeO_2 nanosheets for efficient catalytic oxidation of dichloromethane, Environ. Sci. Technol. 52 (2018) 13430–13437.

[2] Y. Gao, Y. Zhu, L. Lyu, Q. Zeng, X. Xing, C. Hu, Electronic structure modulation of graphitic carbon nitride by oxygen doping for enhanced catalytic degradation of organic pollutants through peroxymonosulfate activation, Environ. Sci. Technol. 52 (2018) 14371–14380.

[3] H. Lin, H. Zhang, L. Hou, Degradation of C. I. Acid Orange 7 in aqueous solution by a novel electro/Fe_3O_4/PDS process, J. Hazard. Mater. 276 (2014) 182–191.

[4] I. Gri, S. Papi, N. Koprivanac, I. Kovai, Kinetic modeling and synergy quantification in sono and photooxidative treatment of simulated dyehouse effluent, Water Res. 46 (2012) 5683–5695.

[5] P.S. Zhang, Photodegradation of Acid Orange 7 in a UV/acetylacetone process, Chemosphere 93 (2013) 2877–2882.

[6] D. Han, J. Wan, Y. Ma, Y. Wang, M. Huang, Y. Chen, D. Li, Z. Guan, Y. Li, Enhanced decolorization of Orange G in a Fe(II)-EDDS activated persulfate process by accelerating the regeneration of ferrous iron with hydroxylamine, Chem. Eng. J. 256 (2014) 316–323.

[7] S.K. Ling, S. Wang, Y. Peng, Oxidative degradation of dyes in water using Co^{2+}/H_2O_2 and Co^{2+}/peroxymonosulfate, J. Hazard. Mater. 178 (2010) 385–389.

[8] M.M. Mian, G. Liu, B. Fu, Y. Song, Facile synthesis of sludge-derived MnO_x-N-biochar as an efficient catalyst for peroxymonosulfate activation, Appl. Catal. B: Environ. 255 (2019), 117765.

[9] H.William Prengle, Experimental rate constants and reactor considerations for the destruction of micropollutants and trihalomethane precursors by ozone with ultraviolet radiation, Environ. Sci. Technol. 17 (1983) 743–747.

[10] R.W. Matthews, Photo-oxidation of organic material in aqueous suspensions of titanium dioxide, Water Res. 20 (1986) 569–578.

[11] T. Olmez-Hanci, I. Arslan-Alaton, S. Gurmen, I. Gafarli, S. Khoei, S. Safaltin, D. Y. Ozcelik, Oxidative degradation of Bisphenol A by carbocatalytic activation of persulfate and peroxymonosulfate with reduced graphene oxide, J. Hazard. Mater. 360 (2018) 141–149.

[12] F. Liu, W. Li, D. Wu, T. Tian, G.C. Zhao, New insight into the mechanism of peroxymonosulfate activation by nanoscaled lead-based spinel for organic matters

degradation: a singlet oxygen-dominated oxidation process, J. Colloid Interface Sci. 572 (2020) 318–327.

[13] Y. Shang, X. Xu, B. Gao, S. Wang, X. Duan, Single-atom catalysis in advanced oxidation processes for environmental remediation, Chem. Soc. Rev. 50 (2021) 5281–5322.

[14] M. Noorisepehr, K. Ghadirinejad, B. Kakavandi, A. Ramazanpour Esfahani, A. Asadi, Photo-assisted catalytic degradation of acetaminophen using peroxymonosulfate decomposed by magnetic carbon heterojunction catalyst, Chemosphere 232 (2019) 140–151.

[15] S.S. Rezaei, B. Kakavandi, M. Noorisepehr, A.A. Isari, S. Zabih, P. Bashardoust, Photocatalytic oxidation of tetracycline by magnetic carbon-supported TiO$_2$ nanoparticles catalyzed peroxydisulfate: Performance, synergy and reaction mechanism studies, Sep. Purif. Technol. 258 (2021), 117936.

[16] Z. Frontistis, G. Trakakis, L. Sygellou, C. Galiotis, D. Mantzavinos, Graphene: a new activator of sodium persulfate for the advanced oxidation of parabens in water, Water Res. 126 (2017) 111–121.

[17] S. Indrawirawan, H. Sun, X. Duan, S. Wang, Nanocarbons in different structural dimensions (0–3D) for phenol adsorption and metal-free catalytic oxidation, Appl. Catal. B Environ. 179 (2015) 352–362.

[18] E.T. Yun, H.Y. Yoo, H. Bae, H.I. Kim, J. Lee, Exploring the role of persulfate in the activation process: radical precursor versus electron acceptor, Environ. Sci. Technol. 51 (2017) 10090–10099.

[19] R. Li, M. Cai, Z. Xie, Q. Zhang, Y. Zeng, HaijinLiu, G. Liu, W. Lv, Construction of heterostructured CuFe$_2$O$_4$/g-C$_3$N$_4$ nanocomposite as an efficient visible light photocatalyst with peroxydisulfate for the organic oxidation, Appl. Catal. B: Environ. 244 (2019) 974–982.

[20] X. Duan, C. Su, J. Miao, Y. Zhong, Z. Shao, S. Wang, H. Sun, Insights into perovskite-catalyzed peroxymonosulfate activation: maneuverable cobalt sites for promoted evolution of sulfate radicals, Appl. Catal. B: Environ. 220 (2018) 626–634.

[21] F. Wang, H. Fu, F.X. Wang, X.W. Zhang, P. Wang, C. Zhao, C.C. Wang, Enhanced catalytic sulfamethoxazole degradation via peroxymonosulfate activation over amorphous CoS$_x$@SiO$_2$ nanocages derived from ZIF-67, J. Hazard. Mater. 423 (2022), 126998.

[22] J. Hang, X.H. Yi, C.C. Wang, H. Fu, P. Wang, Y. Zhao, Heterogeneous photo-Fenton degradation toward sulfonamide matrix over magnetic Fe$_3$S$_4$ derived from MIL-100 (Fe), J. Hazard. Mater. 424 (2022), 127415.

[23] A. Du, H. Fu, P. Wang, C. Zhao, C.C. Wang, Enhanced catalytic peroxymonosulfate activation for sulfonamide antibiotics degradation over the supported CoSx-CuSx derived from ZIF-L(Co) immobilized on copper foam, J. Hazard. Mater. 426 (2022), 128134.

[24] M. Zhang, C. Han, W. Chen, W. Luo, Y. Cao, G. Qian, X. Zhou, X. Duan, S. Wang, X. Duan, Active sites and reaction mechanism for N-doped carbocatalysis of phenol removal, Green Energy Environ. 5 (2020) 444–452.

[25] Y. Shang, T. Wang, Y. Xiao, Z. Dong, X. Li, B. Li, Constructing BiOBr/CoO$_x$/g-C$_3$N$_4$ Z-scheme photocatalyst with CoO$_x$ as both redox mediator and cocatalyst for phenol degradation, J. Alloy. Compd. 875 (2021), 159998.

[26] W. Xu, W. Xue, H. Huang, J. Wang, C. Zhong, D. Mei, Morphology controlled synthesis of α-Fe$_2$O$_{3-x}$ with benzimidazole-modified Fe-MOFs for enhanced photo-Fenton-like catalysis, Appl. Catal. B: Environ. 291 (2021) 120129.

[27] A. Wang, J. Li, T. Zhang, Heterogeneous single-atom catalysis, Nat. Rev. Chem. 2 (2018) 65–81.

[28] X.F. Yang, A. Wang, B. Qiao, J. Li, J. Liu, T. Zhang, Single-atom catalysts: a new frontier in heterogeneous catalysis, Acc. Chem. Res. 46 (2013) 1740.

[29] B. Qiao, A. Wang, X. Yang, L.F. Allard, Z. Jiang, Y. Cui, J. Liu, J. Li, Z. Tao, Single-atom catalysis of CO oxidation using Pt$_1$/FeO$_x$, Nat. Chem. 3 (2011) 634–641.

[30] Y. Fan, S. Liu, Y. Yi, H. Rong, J. Zhang, Catalytic nanomaterials toward atomic levels for biomedical applications: from metal clusters to single-atom catalysts, ACS Nano 15 (2021) 2005–2037.

[31] Y. Shi, Y. Zhou, Y. Lou, Z. Chen, H. Xiong, Y. Zhu, Homogeneity of supported single-atom active sites boosting the selective catalytic transformations, Adv. Sci. (2022), 2201520.

[32] Y. Lou, J. Xu, Y. Zhang, C. Pan, Y. Dong, Y. Zhu, Metal-support interaction for heterogeneous catalysis: from nanoparticles to single atoms, Mater. Today Nano 12 (2020) 10093.

[33] T. Wu, M.M. Melander, K. Honkala, Coadsorption of NRR and HER intermediates determines the performance of Ru-N4 toward electrocatalytic N$_2$ reduction, ACS Catal. 12 (2022) 2505–2512.

[34] H. Gharibi, N. Dalir, M. Jafari, M.J. Parnian, M. Zhiani, Engineering dual metal single-atom sites with the nitrogen-coordinated nonprecious catalyst for oxygen reduction reaction (ORR) in acidic electrolyte, Appl. Surf. Sci. 572 (2022), 151367.

[35] R. Yun, F. Zhan, X. Wang, B. Zhang, T. Sheng, Z. Xin, J. Mao, S. Liu, B. Zheng, Design of binary Cu-Fe sites coordinated with nitrogen dispersed in the porous carbon for synergistic CO$_2$ electroreduction, Small 17 (2021), 2006951.

[36] X. Tang, L. Wang, B. Yang, C. Fei, T. Yao, W. Liu, Y. Lou, Q. Dai, Y. Cai, X.-M. Cao, W. Zhan, Y. Guo, X.-Q. Gong, Y. Guo, Direct oxidation of methane to oxygenates on supported single Cu atom catalyst, Appl. Catal. B: Environ. 285 (2021) 119827.

[37] Y. Lou, F. jiang, W. Zhu, L. Wang, T. Yao, S. Wang, B. Yang, B. Yang, Y. Zhu, X. Liu, CeO$_2$ supported Pd dimers boosting CO$_2$ hydrogenation to ethanol, Appl. Catal. B: Environ. 291 (2021), 120122.

[38] X. Xu, F. Zhan, J. Pan, L. Zhou, L. Su, W. Cen, W. Li, C. Tian, Engineering single-atom Fe-Pyridine N$_4$ sites to boost peroxymonosulfate activation for antibiotic degradation in a wide pH range, Chemosphere 294 (2022), 133735.

[39] Z. Li, K. Li, S. Ma, B. Dang, Q. Meng, Activation of peroxymonosulfate by iron-biochar composites: Comparison of nanoscale Fe with single-atom Fe, J. Colloid Interface Sci. 582 (2020) 598–609.

[40] X. Li, X. Huang, S. Xi, S. Miao, J. Ding, W. Cai, S. Liu, X. Yang, H. Yang, J. Gao, J. Wang, Y. Huang, T. Zhang, B. Liu, Single cobalt atoms anchored on porous N-doped graphene with dual reaction sites for efficient fenton-like catalysis, J. Am. Chem. Soc. 140 (2018) 12469–12475.

[41] X.-H. Yi, H. Ji, C.-C. Wang, Y. Li, Y.-H. Li, C. Zhao, A. Wang, H. Fu, P. Wang, X. Zhao, W. Liu, Photocatalysis-activated SR-AOP over PDINH/MIL-88A(Fe) composites for boosted chloroquine phosphate degradation: Performance, mechanism, pathway and DFT calculations, Appl. Catal. B: Environ. 293 (2021), 120229.

[42] G. Wang, X. Nie, X. Ji, X. Quan, S. Chen, H. Wang, H. Yu, X. Guo, Enhanced heterogeneous activation of peroxymonosulfate by Co and N codoped porous carbon for degradation of organic pollutants: the synergism between Co and N, Environ. Sci.: Nano 6 (2019) 399–410.

[43] J. Yang, D. Zeng, Q. Zhang, R. Cui, M. Hassan, L. Dong, J. Li, Y. He, Single Mn atom anchored on N-doped porous carbon as highly efficient Fenton-like catalyst for the degradation of organic contaminants, Appl. Catal. B: Environ. 279 (2020) 119363.

[44] W. Wang, Y. Zhu, X. Zhu, Y. Zhao, Z. Xue, C. Xiong, Z. Wang, Y. Qu, J. Cheng, M. Chen, M. Liu, F. Zhou, H. Zhang, Z. Jiang, Y. Hu, H. Zhou, H. Wang, Y. Li, Y. Liu, Y. Wu, Biocompatible ruthenium single-atom catalyst for cascade enzyme-mimicking therapy, ACS Appl. Mater. Interfaces 13 (2021) 45269–45278.

[45] G. Boczkaj, A. Fernandes, Wastewater treatment by means of advanced oxidation processes at basic pH conditions: a review, Chem. Eng. J. 320 (2017) 608–633.

[46] F.-X. Wang, C.-C. Wang, X. Du, Y. Li, F. Wang, P. Wang, Efficient removal of emerging organic contaminants via photo-Fenton process over micron-sized Fe-MOF sheet, Chem. Eng. J. 429 (2022), 132495.

[47] Y. Yao, F. Lu, Y. Zhu, F. Wei, X. Liu, C. Lian, S. Wang, Magnetic core-shell CuFe$_2$O$_4$@C$_3$N$_4$ hybrids for visible light photocatalysis of Orange II, J. Hazard. Mater. 297 (2015) 224–233.

[48] Y. Wang, L. Man, Z. Xu, C. Di, Y. Bo, Insights into heterogeneous catalysis of peroxymonosulfate activation by boron-doped ordered mesoporous carbon, Carbon 135 (2018) 238–247.

[49] Y. Yang, P. Zhang, K. Hu, X. Duan, Y. Ren, H. Sun, S. Wang, Sustainable redox processes induced by peroxymonosulfate and metal doping on amorphous manganese dioxide for nonradical degradation of water contaminants, Appl. Catal. B: Environ. 286 (2021).

[50] Zhen Wang, Jin Jiang, Suyan Pang, Yang Zhou, Chaoting Guan, Is sulfate radical really generated from peroxydisulfate activated by iron(II) for environmental decontamination? Environ. Sci. Technol. 52 (2018) 11276–11284.

[51] T. Guo, L. Jiang, K. Wang, Y. Li, H. Huang, X. Wu, G. Zhang, Efficient persulfate activation by hematite nanocrystals for degradation of organic pollutants under visible light irradiation: Facet-dependent catalytic performance and degradation mechanism, Appl. Catal. B: Environ. 286 (2021), 119883.

[52] T. Guo, L. Jiang, H. Huang, Y. Li, X. Wu, G. Zhang, Enhanced degradation of tetracycline in water over Cu-doped hematite nanoplates by peroxymonosulfate activation under visible light irradiation, J. Hazard. Mater. 416 (2021), 125838.

[53] H. Huang, T. Guo, K. Wang, Y. Li, G. Zhang, Efficient activation of persulfate by a magnetic recyclable rape straw biochar catalyst for the degradation of tetracycline hydrochloride in water, Sci. Total Environ. 758 (2021), 143957.

[54] C. Zhao, J. Wang, X. Chen, Z. Wang, H. Ji, L. Chen, W. Liu, C.C. Wang, Bifunctional Bi$_{12}$O$_{17}$Cl$_2$/MIL-100(Fe) composites toward photocatalytic Cr(VI) sequestration and activation of persulfate for bisphenol A degradation, Sci. Total Environ. 752 (2021), 141901.

[55] G. Zhang, J. Zhu, Y. Xu, C. Yang, C. He, P. Zhang, Y. Li, X. Ren, H. Mi, In-plane charge transport dominates the overall charge separation and photocatalytic activity in crystalline carbon nitride, ACS Catal. (2022) 4648–4658.

[56] X. Duan, H. Sun, Y. Wang, J. Kang, S. Wang, N-doping-induced nonradical reaction on single-walled carbon nanotubes for catalytic phenol oxidation, ACS Catal. 5 (2015) 553–559.

[57] H. Zhang, J. Qiu, Degradation of Acid Orange 7 in aqueous solution by a novel electro/Fe^{2+}/peroxydisulfate process, J. Hazard. Mater. 215–216 (2012) 138–145.

[58] X. Chen, J. Chen, X. Qiao, D. Wang, X. Cai, Performance of nano-Co$_3$O$_4$/peroxymonosulfate system: Kinetics and mechanism study using Acid Orange 7 as a model compound, Appl. Catal. B: Environ. 80 (2008) 116–121.

[59] A.J. Medford, A. Vojvodic, J.S. Hummelshøj, J. Voss, F. Abild-Pedersen, F. Studt, T. Bligaard, A. Nilsson, J.K. Nørskov, From the Sabatier principle to a predictive theory of transition-metal heterogeneous catalysis, J. Catal. 328 (2015) 36–42.

[60] J. Yang, P. Li, X. Duan, D. Zeng, Z. Ma, S. An, L. Dong, W. Cen, Y. He, Insights into the role of dual reaction sites for single Ni atom Fenton-like catalyst towards degradation of various organic contaminants, J. Hazard. Mater. 430 (2022), 128463.

[61] P. Ogilby, Singlet oxygen: there is indeed something new under the sun, Chem. Soc. Rev. 39 (2010) 3181–3209.